Chinese Chemical Letters 35 (2024) 108519

Contents lists available at ScienceDirect

Chinese Chemical Letters

journal homepage: www.elsevier.com/locate/cclet

Synergy of phosphorus vacancies and build-in electric field into NiCo/NiCoP Mott-Schottky integrated electrode for enhanced water splitting performance

Xiaochen Zhang, Hui Xue*, Jing Sun, Niankun Guo, Tianshan Song, Jiawen Sun, Yi-Ru Hao, Qin Wang*

College of Chemistry and Chemical Engineering, Inner Mongolia University, Hohhot 010021, China

ARTICLE INFO

Article history:
Received 2 March 2023
Revised 4 April 2023
Accepted 26 April 2023
Available online 1 May 2023

Keywords:
Mott-Schottky
Build-in electric field
Phosphorus vacancies
Phosphides
Overall water splitting

ABSTRACT

Vacancy engineering and Mott-Schottky heterostructure can accelerate charge transfer, regulate adsorption energy of reaction intermediates, and provide additional active sites, which are regarded as valid means for improving catalytic activity. However, the underlying mechanism of synergistic regulation of interfacial charge transfer and optimization of electrocatalytic activity by combining vacancy and Mott-Schottky junction remains unclear. Herein, the growth of a bifunctional NiCo/NiCoP Mott-Schottky electrode with abundant phosphorus vacancies on foam nickel (NF) has been synthesized through continuous phosphating and reduction processes. The obtained NiCo/NiCoP heterojunctions show remarkable OER and HER activities, and the overpotentials for OER and HER are as low as 117 and 60 mV at 10 mA/cm^2 in 1 mol/L KOH, respectively. Moreover, as both the cathode and anode of overall water splitting, the voltage of the bifunctional NiCo/NiCoP electrocatalyst is 1.44 V at 10 mA/cm^2, which are far exceeding the benchmark commercial electrodes. DFT theoretical calculation results confirm that the phosphorus vacancies and build-in electric field can effectively accelerate ion and electron transfer between NiCo alloy and NiCoP semiconductor, tailor the electronic structure of the metal centers and lower the Gibbs free energy of the intermediates. Furthermore, the unique self-supported integrated structure is beneficial to facilitate the exposure of the active site, avoid catalyst shedding, thus improving the activity and structural stability of NiCo/NiCoP. This study provides an avenue for the controllable synthesis and performance optimization of Mott-Schottky electrocatalysts.

Transition metal phosphides (TMPs) are considered to be feasible alternatives to noble metal catalysts due to their abundant resources, low price, and adjustable composition/structure [1,2]. The doping of P atoms in the metal lattice can effectively increase the interatomic distance and significantly induce the contraction of D-band, which makes the electronic characteristics of phosphide similar to those of noble metals [3]. In addition, the high electronegativity of the P atom is beneficial to attract the electrons of the metal, thus facilitating the rapid charge transfer [4,5]. Based on this, the adjustable phase composition and unique electronic structure endow TMPs with excellent catalytic activity, which have been regarded as a promising class of electrocatalytic materials. However, TMPs still suffer from low catalytic activity and poor stability, and the electrical conductivity decreases significantly with the increase of H coating, thus seriously affecting their intrinsic catalytic activity [6]. Therefore, it remains a challenge to tailor the electronic structure and charge transfer of TMPs to further improve the catalytic activity and stability.

Mott-Schottky heterojunctions, which are formed by the efficient integration of conductor and semiconductor materials, have attracted much attention due to the rapid electron transfer, appropriate adsorption energy of intermediate, and excellent electrocatalytic activity [7]. In this type of heterostructure, the conductor part is usually composed of metal or alloys, and transition metal oxides, sulfides, phosphides, and carbon-nitrogen (C–N) materials are often regarded as semiconductor [8–10]. The Schottky effect at the conductor-semiconductor interface can induce the formation of built-in electric fields to markedly enhance the electron transport. The band gap, work function and electrode potential of the semiconductor is conspicuously lower than that of the metal conductor. Based on the difference of their work functions, electrons in semiconductors spontaneously transfer to metal conductors

* Corresponding authors.
E-mail addresses: hxue@imu.edu.cn (H. Xue), qinwang@imu.edu.cn (Q. Wang).

https://doi.org/10.1016/j.cclet.2023.108519
1001-8417/

through heterogeneous interfaces, and electron holes are enriched at the semiconductor side. Benefit from abundant heterogeneous interfaces and build-in electric field, an enhanced electrocatalytic activity can be achieved by optimizing the adsorption energy of intermediates and triggering the redistribution of interfacial charge [11–13]. Furthermore, vacancy defects act as a vital function in regulating the activity of catalysts [14,15]. The defect can reduce the potential barrier and promote the adsorption/desorption of H_2O molecules or reaction intermediates on the surface of the electrocatalyst, thus optimizing the reaction kinetics. Besides, the directly growth of Mott-Schottky integrated electrode on self-supporting supports (nickel foam, carbon cloth, *etc.*) is more conducive to gas production and deaeration, which can effectively prevent the catalysts from falling off during the reaction process. Therefore, the electrocatalytic activity and stability of the TMPs can be significantly promoted by the construction of Mott-Schottky integrated electrode and vacancy defects. However, the underlying mechanism of synergistic regulation of interfacial charge transfer and optimization of electrocatalytic activity by combining vacancy and Mott-Schottky heterojunction remains unclear.

Herein, a 3D nanorod NiCo/NiCoP Mott-Schottky heterostructure electrodes with phosphorus vacancy-rich directly grown on nickel foam were successfully developed through sequential hydrothermal, phosphating, and reduction processes. The obtained NiCo/NiCoP heterojunctions endow the lowest overpotentials for both OER and HER at different current densities. In detail, the OER and HER overpotentials are as low as 117, 232, 276 mV and 60, 128, 195 mV at 10, 50 and 100 mA/cm^2, respectively. In addition, as both the cathode and anode of overall water splitting, the voltage of the bifunctional NiCo/NiCoP electrocatalyst is 1.44, 1.57 and 1.63 V at current densities of 10, 50 and 100 mA/cm^2, which are far exceeding the benchmark commercial electrodes. The DFT theoretical calculation results reveal that Mott-Schottky heterointerface and phosphorus defects alleviate the competitive adsorption of hydroxyl and H_2O with steric hindrance, and effectively regulate the electronic structure of atoms near Fermi level. In addition, the unique self-supporting integrated structure is beneficial to improve the conductivity and avoid the catalyst from falling off, thus improving the activity and structural stability.

The NiCo/NiCoP Mott-Schottky heterostructure electrodes were successfully fabricated by sequential hydrothermal, phosphating, and reduction processes (Fig. 1a). The XRD pattern in Fig. S1 (Supporting information) indicates that the NiCo-MOF precursor has been developed. In Fig. 1b and Fig. S2 (Supporting information), four diffraction peaks located at 30.6°, 40.9° 47.5° and 54.5° belong to the (110), (111), (210) and (300) crystal planes of NiCoP (PDF#71–2336). In addition, the peaks of NiCo alloy (PDF#15–0806) can also be observed at 44.5°, 51.8° and 76.3°, which are attributed to the (111), (200), and (220) planes, indicating the Mott-Schottky heterojunction structure of NiCo/NiCoP eventually formed. The effect of NaH_2PO_2 amount on phosphating was also studied. The degree of phosphating gradually increased with the increase of the amount of $NaH_2PO_2{\cdot}H_2O$ (from 0.2 g to 0.8 g), and the peak intensity of NiCoP became stronger (Fig. S3 in Supporting information). The morphological features of the samples are described in detail by SEM. The NF@NiCo-MOF precursor is composed of some smooth-surfaced nanorods with the diameter of 220 nm grown on nickel foam substrate (Fig. 1c and Fig. S4 in Supporting information). The overall morphology of NiCoP is consistent with NF@NiCo-MOF, but phosphatization result in the partial fracture of NiCoP nanorods (Fig. 1d and Fig. S5 in Supporting information). After the reduction process, the basic morphology of NiCo/NiCoP remains intact and the surface becomes rough (Fig. 1e and Fig. S6 in Supporting information). The rough surface has greater contact with the electrolyte, enriching the edge sites involved in electrochemical reactions, which is beneficial to improve the electrocatalytic activity [16]. The TEM (Fig. 1f) and HR-TEM (Figs. 1g-i) results reveal that the lattice fringe spacings of 0.19 and 0.22 nm belong to the (210) and (111) crystal plane of NiCoP, and the (111) crystal plane of NiCo with the spacing of 0.20 nm can also be detected, further indicating the NiCo alloy and NiCoP Mott-Schottky heterojunction was successfully synthesized. In addition, there are some lattice site deletions in the crystal plane of NiCoP, which may be caused by the formation of vacancy defects (Fig. 1h). The SAED pattern (Fig. 1j) clearly reveals a polycrystalline phase of NiCo/NiCoP catalyst. The element mapping images and scanning transmission electron microscopy-energy dispersive X-ray (STEM-EDX) spectra confirm that the Co, Ni, P, O, C and N elements are evenly distributed in NiCo/NiCoP Mott-Schottky heterojunction (Fig. 1k and Fig. S7 in Supporting information).

The surface chemical state and electronic interaction of the obtained NiCo/NiCoP catalyst has been characterized by using XPS. As shown in Fig. 2a, the XPS results indicate that the coexistence of Ni, Co, P, O, C and N elements in NiCo/NiCoP catalyst. The Ni 2p XPS spectra (Fig. 2b) show the peaks at 856.9 and 874.6 eV in three samples correspond to $2p_{3/2}$ and $2p_{1/2}$ of Ni^{2+}, accompanied by two satellite peaks with binding energies of 861 and 880 eV [17,18]. For NiCo/NiCoP catalyst, another two peaks are ascribed to Ni^0 (853.4 and 870.6 eV) can be observed, which is caused by the partial reduction during heat treatment [19,20]. Similarly, in the XPS spectra of Co 2p, two peaks of binding energies at 782.5 and 798.4 eV are assigned to $2p_{3/2}$ and $2p_{1/2}$ of Co^{2+} species, respectively. And two satellite peaks of 786.9 (Co $2p_{3/2}$ Sat.) and 804 eV (Co $2p_{1/2}$ Sat.) can also be detected [21,22]. Furthermore, Co^0 peaks with the binding energy of 778.8 and 793.4 eV further indicates that metallic Co exists in NiCo/NiCoP (Fig. 2c) [23,24]. According to the literature, the peak of Ni 2p and Co 2p in NiCo/NiCoP are shifted compared with NiCoP, which means that the electron density of nickel and cobalt species decreases after introducing more phosphorus vacancies. In addition, it also shows that there is a strong electronic interaction between NiCo and NiCoP through the established epitaxial heterogeneous interface [25,26]. Fig. 2d shows the presence of P $2p_{3/2}$ and P $2p_{1/2}$ with the characteristic peaks of 129.4 and 130.1 eV, respectively [27]. In addition, a huge P-O peak at 134.4 eV can be detected, which is mainly due to the oxidation of the NiCoP surface to form an amorphous phosphate layer when exposed to air [28]. Meanwhile, the peaks of P 2p in NiCo/NiCoP are negatively shifted by 0.1 eV compared with NiCoP catalyst, and the peak intensities of both P-O and P 2p decreased, which may indicate the formation of phosphorus vacancy defects in NiCo/NiCoP sample [29–31]. In Fig. 2e, the O 1s spectrum can be deconvolved into two characteristic peaks. Specifically, the peak at 531.7 eV is attributed to lattice oxygen (O_L^{2-}), and the peak at 533 eV is attributed to water molecules adsorbed on the surface [32–35]. In the N 1s spectra (Fig. S8a in Supporting information), four different kinds of nitrogen, including pyridine-N (398.5 eV), pyrrole-N (399.7 eV), graphite-N (401.4 eV) and oxide-N (402.9 eV) can be assigned [36]. In the C 1s XPS spectra of Fig. S8b, the peak of C = C, C–N and C–O are observed [37]. The presence of P vacancies is further determined by electron paramagnetic resonance (EPR) spectroscopy (Fig. 2f). The broad peak signal (g~2.018) is caused by the existence of unsaturated electrons, which are proven by previous studies to be phosphorus vacancies in NiCo/NiCoP sample [38]. It can be found that the signal intensity of NiCo/NiCoP is higher than that of NiCoP, indicating that partial reduction under Ar/H_2 atmosphere can create more vacancy defects. Raman spectra show that the I_D/I_G values of NiCo/NiCoP and NiCoP are 1.22 and 1.03, respectively, which indicates that the carbon graphitization and disorder of NiCo/NiCoP catalyst are higher, so it has better conductivity and electrochemical performance (Fig. S9 in Supporting information) [39]. In order to deeply study the electrical function of interface contact between NiCo and NiCoP, the Mott-Schottky curves

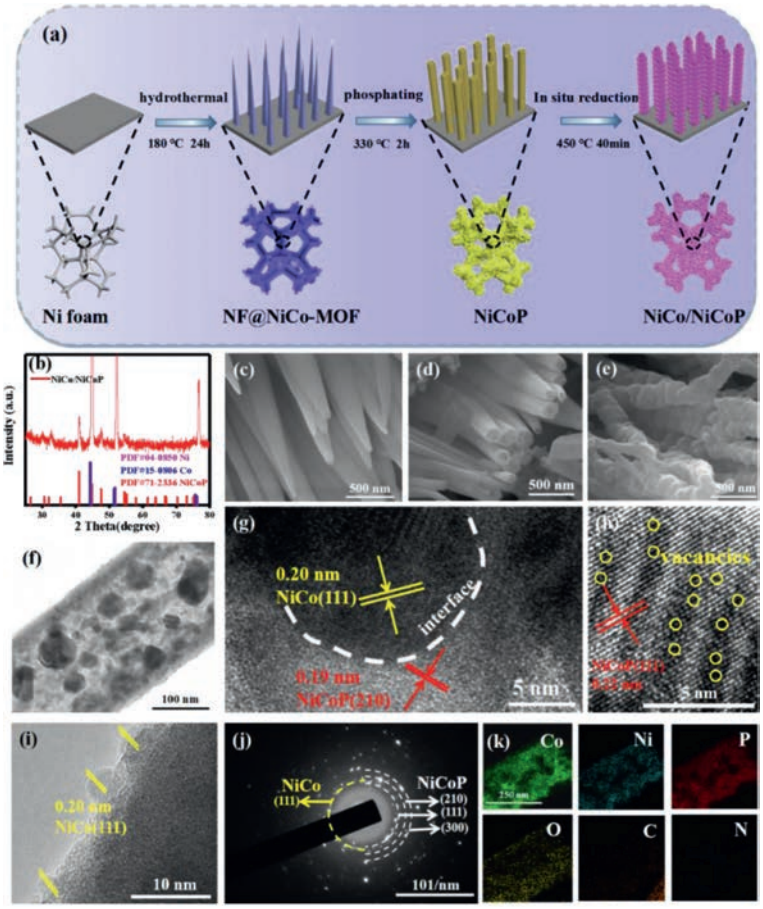

Fig. 1. (a) Schematic diagram for the synthesis of NiCo/NiCoP Mott-Schottky heterojunction. (b) XRD pattern of NiCo/NiCoP. SEM images of (c) NiCo-MOF/NF, (d) NiCoP, (e) NiCo/NiCoP. (f) TEM images; (g-i) HR-TEM, (j) SAED pattern, (k) elemental mapping of NiCo/NiCoP.

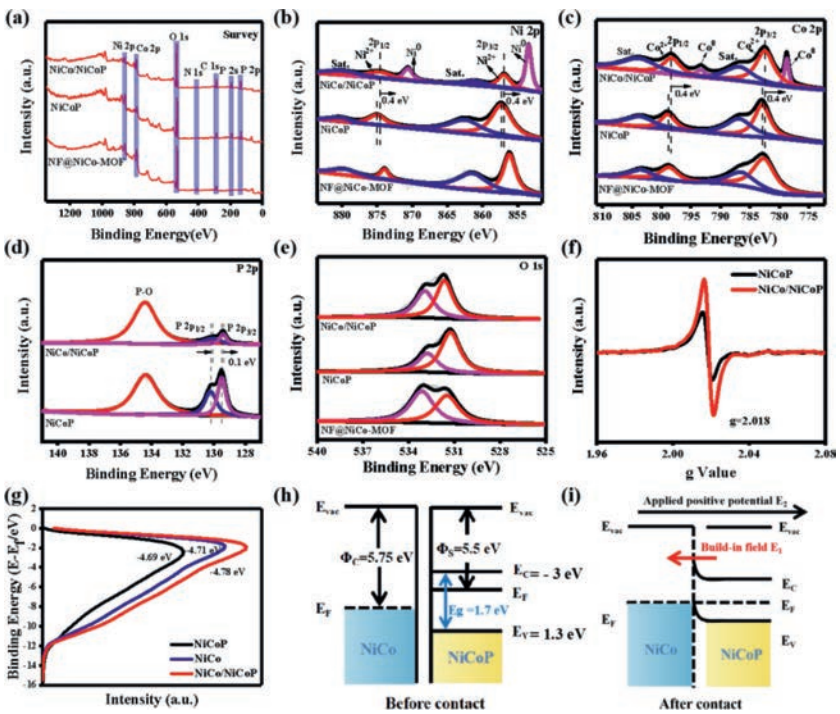

Fig. 2. XPS spectra of obtained catalysts. (a) XPS survey, (b) Ni 2p, (c) Co 2p, (d) P 2p, (e) O 1s. (f) EPR spectra. (g-i) Energy diagrams of NiCo and NiCoP (Φ: Work function, E_F: Fermi level, E_{vac}: Vacuum level, E_V: Valence band, E_C: Conduction band).

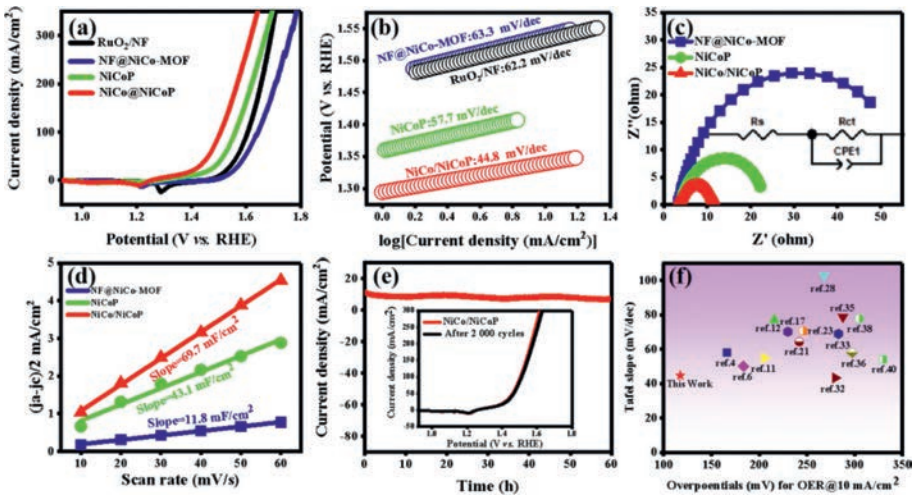

Fig. 3. (a) OER polarization curves. (b) Tafel plots. (c) Electrochemical impedance spectroscopy. (d) C_{dl} values. (e) Stability tests of NiCo/NiCoP. (f) Comparison of OER activities.

of NiCoP was tested at different frequencies in 0.5 mol/L Na_2SO_4 solution (Fig. S10a in Supporting information). The flat band (FB) potential (V_{FB}) of NiCoP is −1.3 V (*vs.* RHE, @−3.2 eV *vs.* vacuum level). In addition, the difference between the conduction band (CB) potential (E_C) of NiCoP and its V_{FB} (Fermi level) is 0.2 eV, so the E_C of NiCoP is −3 eV. The ultraviolet-visible spectrum (UV–vis) of NiCoP sample was tested, and its band gap E_g is 1.7 eV by extrapolation (Fig. S10b in Supporting information), so the valence band *E*v is 1.3 eV [40]. Furthermore, we conducted the ultraviolet photoelectron spectroscopy (UPS) test. As shown in Figs. 2g-i and Fig. S11 (Supporting information), the work function values of metallic NiCo and semiconducting NiCoP are 5.75 and 5.5 eV, respectively, resulting in a Mott-Schottky barrier between NiCo and NiCoP. Electrons spontaneously transfer from NiCoP to NiCo until the Fermi levels of both sides reach a dynamic equilibrium. As a result, the electrons gather in the NiCo region and have nucleophilicity, and the holes gather in the NiCoP region and have electrophilicity. The built-in electric field and the charge redistribution at the NiCo/NiCoP heterointerface can significantly accelerate charge transfer, enhance the intrinsic catalytic activity and improve the reaction kinetics [41,42].

The catalytic performance of the samples had been systematacially studied based on the linear sweep voltammetry (LSV) experiments. The NiCo/NiCoP catalyst delivers an outstanding OER activity with the lowest overpotentials of 117, 232 and 276 mV at the current densities of 10, 50 and 100 mA/cm^2, much lower than NiCoP, NF@NiCo-MOF, and the commercial RuO_2/NF catalyst (Fig. 3a and Fig. S12 in Supporting information). The Tafel slope of 44.8 mV/dec for NiCo/NiCoP is obviously smaller than those of NiCoP (57.7 mV/dec), NiCo-MOF/NF (63.3 mV/dec), and RuO_2/NF (62.2 mV/dec), indicating the fastest OER kinetic rate (Fig. 3b). Furthermore, the electrochemical impedance spectroscopy (EIS) test can reflect the charge transfer ability and reaction kinetics of the samples, and the results show that the NiCo/NiCoP catalyst with the minimum R_{ct} has a higher charge transfer rate during the OER process (Fig. 3c). The electrochemically active surface areas (ECSA) of the catalysts are proportional to the double-layer capacitance (C_{dl}), and C_{dl} can be obtained by cyclic voltammetry (CV) test at different scanning rates (10–60 mV/s) in the non-Faraday voltage range of 0-0.1 V (Fig. S13 in Supporting information). The C_{dl} values for NiCo/NiCoP, NiCoP, and NiCo-MOF/NF are calculated to be 69.7, 43.1 and 11.8 mF/cm^2, respectively. The largest C_{dl} value indicates that the NiCo/NiCoP heterojunction has the highest ECSA (Fig. 3d). Therefore, the phosphorus vacancy and built-in electric field in the NiCo/NiCoP Mott-Schottky heterostructure can effectively accelerate electron transfer, tailor electron structure, and significantly improve electrocatalytic activity. As shown in Fig. 3e, the stability of NiCo/NiCoP is evaluated by constant chronoamperometry.

After 60 h long-term stability test, the current density of the NiCo/NiCoP catalyst has almost no change. Moreover, the LSV curves show a slight change before and after 2000 cycles, further indicating the excellent OER stability of NiCo/NiCoP heterojunction. The excellent stability of NiCo/NiCoP electrocatalyst may be attributed to the self-supporting heterogeneous structure electrode and the formation of amorphous phosphate layer on the surface. Fig. 3f and Table S1 (Supporting information) demonstrate that the NiCo/NiCoP catalysts perform very well compared to recently reported OER electrocatalysts in alkaline electrolytes.

The HER performance of the obtained catalysts was also analyzed. The NiCo/NiCoP catalyst shows the optimal HER activity among the contrast samples with the lower overpotentials of 60, 128 and 158 mV at 10, 50 and 100 mA/cm^2, respectively (Fig. 4a and Fig. S14 in Supporting information). In Fig. 4b, the corresponding Tafel slope of NiCo/NiCoP sample (53.4 mV/dec) is significantly lower than NiCoP (92.2 mV/dec) and NF@NiCo-MOF (214.5 mV/dec), indicating the faster kinetic rate of HER reaction. Fig. 4c shows that the NiCo/NiCoP has the smallest R_{ct} with the strongest charge transfer capability during HER. Fig. S15 (Supporting information) are the CV tests of the synthesized catalysts with different scan rates in the voltage range of −0.874 ∼ −0.774 V. The C_{dl} value of NiCo/NiCoP is calculated to be 59.1 mF/cm^2, which is far higher than those of NiCoP (23.1 mF/cm^2) and NF@NiCo-MOF (8.7 mF/cm^2), indicating that the phosphorus vacancy and Mott-Schottky heterostructure can expose more activity sites (Fig. 4d). The stability test results show that the NiCo/NiCoP remains stable at 10 mA/cm^2 for 60 h, and the 2000 CV cycling tests also manifest the outstanding HER stability of NiCo/NiCoP (Fig. 4e). Fig. 4f and Table S2 (Supporting information) present the activity comparison of NiCo/NiCoP with other reported HER electrocatalyst in alkaline electrolytes.

Considering the excellent OER and HER activities of NiCo/NiCoP catalyst, the performance of the overall water splitting in a two-electrode system was tested. The LSV curves of NiCo/NiCoP||NiCo/NiCoP and RuO_2/NF||Pt/C/NF are measured in Fig. 5a. It can be legibly seen that H_2 and O_2 bubbles are formed on the cathode and anode (inset image), respectively, proving the rapid total water splitting reaction on the NiCo/NiCoP surface. Notably, NiCo/NiCoP||NiCo/NiCoP cells reach current densities

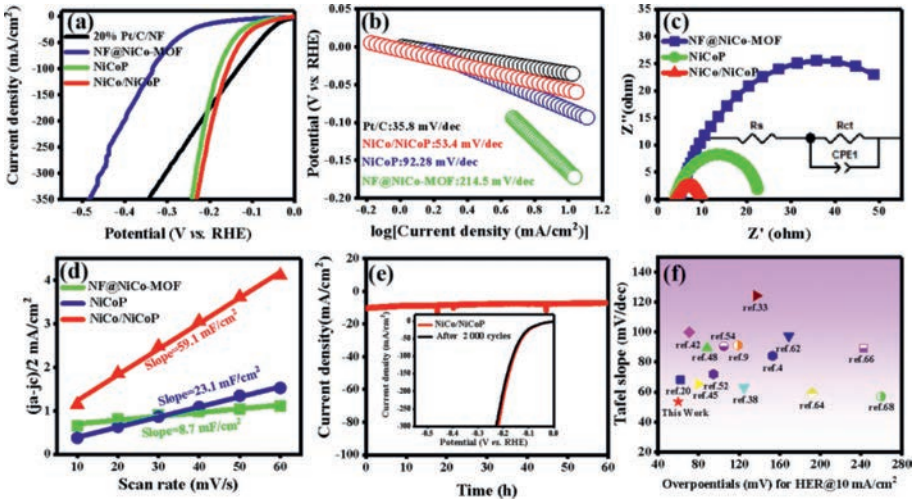

Fig. 4. (a) HER polarization curves. (b) Tafel plots. (c) Electrochemical impedance spectroscopy. (d) C_{dl} values. (e) Stability tests of NiCo/NiCoP. (f) Comparison of HER activities.

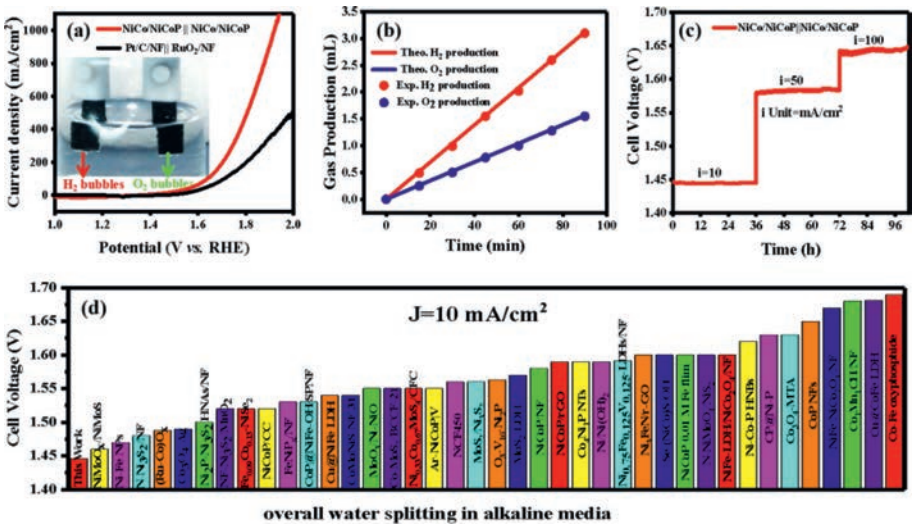

Fig. 5. (a) LSV polarization curves (inset image shows a digital photograph of the two-electrode system). (b) Time-gas evolution amounts for evaluating the Faradic efficiency. (c) Long-term stability test. (d) Comparison of cell votages at 10 mA/cm^2 of recently reported overall water splitting electrocatalysts.

of 10, 50 and 100 mA/cm^2 with only voltages of 1.44, 1.57 and 1.63 V, while RuO_2/NF||Pt/C/NF requires 1.60, 1.75, 1.82 V accordingly (Fig. S16 in Supporting information). Fig. 5b shows that the amount of generated O_2 and H_2 gas is basically consistent with the theoretical value, indicating that Faraday efficiency (FE) is assessed to be close to 100%. Fig. 5c reflects the continuous and effective electrocatalytic reaction of oxygen and hydrogen evolution by NiCo/NiCoP electrode at 10, 50 and 100 mA/cm^2, which shows outstanding catalytic activity and stability for overall water splitting. As predicted, such low voltages for water splitting are quite competitive among the reported materials in Fig. 5d and Table S3 (Supporting information).

The surface reconstruction of NiCo/NiCoP Mott-Schottky heterojunction after OER process was investigated by XRD, XPS and TEM. The XRD spectra in Fig. 6a show that the intensity of diffraction peaks is weakened after OER, but no new diffraction peak appears, indicating that the structure of NiCo/NiCoP Mott-Schottky is basically intact, and some substances with poor crystallinity may be formed on its surface. The SEM image after OER indicates that the morphology becomes irregular, but it still maintains a rod shape (Fig. 6b). As can be seen from HRTEM images and selected area electron diffraction (Fig. 6c), the lattice spacings of 0.32, 0.23, 0.24 and 0.20 nm correspond to (120) and (111) crystal planes of CoOOH (PDF#26–0480), (101) crystal plane of NiOOH (PDF#06–0075) and (111) facet of NiCo alloy (PDF#15–0806), respectively. The results reveal that the surface reconstruction mainly occurs on NiCoP surface and corresponding hydroxyl oxides are formed. The surface composition of NiCo/NiCoP after OER was also studied by XPS. The Ni, Co, P, C, N and O elements can be observed from the survey, and the peak intensity of P is lower than that before the reaction (Fig. S17a in Supporting information). In addition, in the XPS spectra of Ni 2p and Co 2p, the peak intensities of Ni^0 and Co^0 are obviously reduced, and the intensities of Ni^{3+} (858 eV) and Co^{3+} (783.7 eV) are enhanced, which further indicate that Ni and Co are partially oxidized to high valence state during OER process (Figs. 6d and e) [43,44]. In the P 2p XPS spectrum (Fig. 6f), the P-M bonding disappears, indicating that the NiCoP has undergone surface reconstruction. In the XPS spectrum of O 1s in Fig. S17b (Supporting information), the characteristic peak at 529.8 eV corresponds to the bonding between metal and hydroxyl (M-OH), which further proves that the surface of the catalyst is reconstructed to generate hydroxyl oxide during OER [45].

In order to investigate the effect of Mott-Schottky heterogeneous interface and phosphorus vacancy on OER/HER activity of

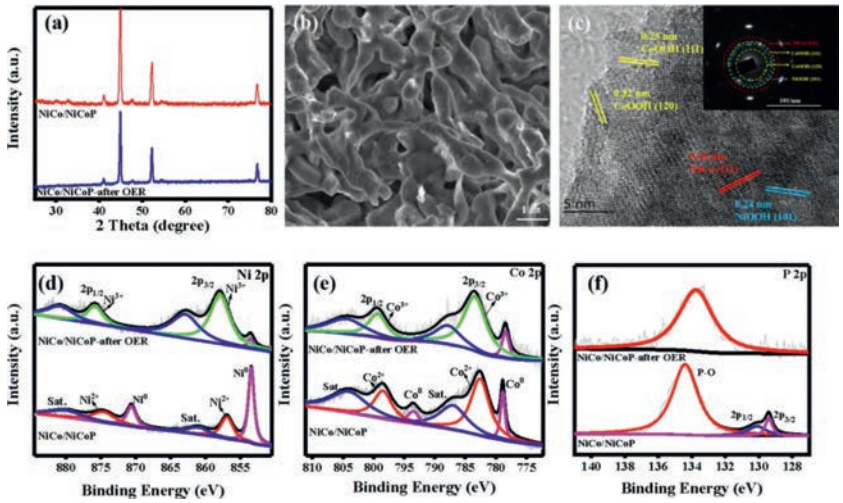

Fig. 6. After OER reaction of NiCo/NiCoP sample (a) XRD pattern; (b) SEM image; (c) TEM image (The illustration is SAED pattern); (d) Ni 2p; (e) Co 2p; (f) P 2p.

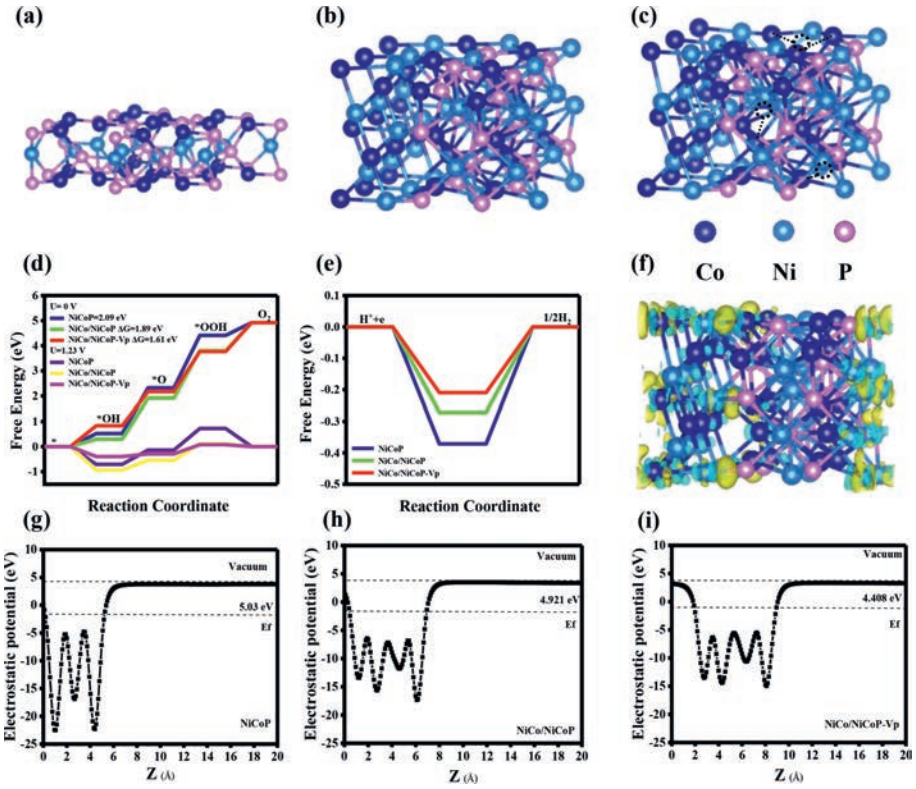

Fig. 7. The model structures of (a) NiCoP, (b) NiCo/NiCoP, (c) NiCo/NiCoP-Vp. (d) OER Gibbs free energy distribution of different catalysts at 0 V and 1.23 V. (e) HER Gibbs free energy distribution of different catalysts at 0 V. (f) The differential charge density of NiCo/NiCoP-Vp structure (The isosurface value is 0.005 eV/Å^3, yellow is the region of electron accumulation and blue is the region of electron dissipation). (g-i) Electrostatic potential distribution diagram.

NiCo/NiCoP catalyst, three density functional theory (DFT) calculation models, including NiCoP, NiCo/NiCoP and NiCo/NiCoP Mott-Schottky heterojunction with phosphorus vacancy (NiCo/NiCoP-Vp) have been established in this paper (Figs. 7a-c). The relationship between the water decomposition process and the adsorption behavior of intermediates and their corresponding roles in the overall alkaline OER/HER rate are studied. For OER processes with four-electron reaction mechanisms, the Gibbs free energy (ΔG) of oxygen-containing intermediates (OH*, O*, OOH*) is used to estimate electrocatalytic activity, and the step with the highest energy barrier is the rate-control step of the reaction [46,47]. The OER step diagram shows that the rate control step of the three models are *O →*OOH process (Fig. 7d and Fig. S18 in Supporting information). Among them, NiCo/NiCoP-Vp Mott-Schottky heterojunction has the smallest free energy barrier (1.61 eV), which is lower than NiCoP (2.09 eV) and NiCo/NiCoP (1.89 eV). The decrease of ΔG means that phosphorus vacancy can affect the charge transfer of Mott-Schottky heterostructure, thus improving the interaction between catalyst and OER intermediate. On the other hand, it is well known that HER process in alkaline environment includes two continuous steps: hydrolytic ionization and hydrogen adsorption, and the activation energy barrier of water decomposition plays an important role in determining the overall HER kinetic rate [48]. Generally speaking, ΔG_{H^*} is consid-

ered to be an important parameter to analyze HER activity [49]. Fig. 7e shows the ΔG_{H^*} of HER process at NiCoP, NiCo/NiCoP, and NiCo/NiCoP-Vp active centers. The NiCo/NiCoP-Vp with the lowest ΔG_{H^*} and close to the ideal ΔG_{H^*} at 0 eV, providing more favorable hydrogen adsorption kinetics than NiCoP and NiCo/NiCoP, and thus showing the optimal HER activity (Fig. S19 in Supporting information). In addition, the differential charge density of NiCo/NiCoP-Vp structure in Fig. 7f reveals that the formation of Mott-Schottky heterojunction and the phosphorus vacancy defect can effectively enrich the electrons on the NiCo side, improve the adsorption capacity of NiCo/NiCoP-Vp to the reaction intermediates, and then significantly enhance the overall water splitting performance. Figs. 7g-i show the electrostatic potential distribution of NiCoP, NiCo/NiCoP, and NiCo/NiCoP-Vp, in which the electrostatic potential of NiCo/NiCoP-Vp is 4.408 eV, which is lower than that of NiCo/NiCoP (4.921 eV) and NiCoP (5.03 eV). It is further proved that NiCo/NiCoP-Vp has the lowest potential barrier [50,51]. Therefore, DFT theoretical calculations manifest that the synergistic effect of Mott-Schottky heterojunction and phosphorus vacancy defect effectively regulates the inherent charge distribution of exposed atoms at the NiCo/NiCoP-Vp heterointerface and reduces the Gibbs free energy of the reaction intermediates, thus significantly optimizing the OER/HER performance.

As a bifunctional electrocatalyst, NiCo/NiCoP shows the advantages of high activity and stability towards alkaline OER, HER and overall water splitting. The outstanding electrocatalytic property may be derived from the following aspects (Scheme 1): (1) The built-in electric field induced by Mott-Schottky heterojunction can effectually tailor the interface electronic structure, optimize the redistribution of charge, and enhance the reactivity. (2) The abundant phosphorus vacancies are beneficial to accelerate electron transfer, provide more active sites, and improve the conductivity of the catalyst, thus significantly promoting the electrocatalytic performance. (3) The unique self-supported integrated structure can facilitate the exposure of the active site, avoid catalyst shedding, and further improve the activity and structural stability of NiCo/NiCoP catalyst.

In summary, we successfully achieved the growth of nanorod-shaped NiCo/NiCoP Mott-Schottky heterostructure electrocatalysts with phosphorus vacancies on the surface of nickel foam. The obtained catalyst exhibits the superior OER, HER, and water splitting performance. Specifically, the NiCo/NiCoP sample needs low overpotentials of 117 mV (OER) and 60 mV (HER) to achieve a current density of 10 mA/cm^2. In addition, the NiCo/NiCoP heterostructure delivers preeminent overall water splitting performance with low cell voltage (1.44 V) and excellent catalytic stability. Combined with experimental and theoretical calculation results show that the electrocatalytic activity is effectively enhanced by the formation of Mott-schottky heterostructure and the introduction of phosphorus vacancy defects.

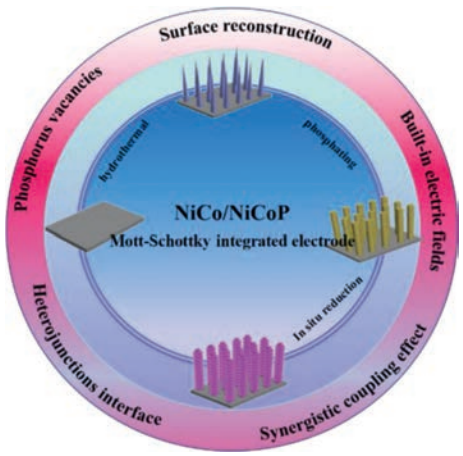

Scheme 1. Schematic diagram of catalytic performance over NiCo/NiCoP.

Declaration of competing interest

There are no conflicts to declare.

Acknowledgments

This project was financially supported by the National Natural Science Foundation of China (NSFC, Nos. 22269015, 22205119), Natural Science Foundation of Inner Mongolia Autonomous Region of China (Nos. 2021ZD11, 2019BS02015).

Supplementary materials

Supplementary material associated with this article can be found, in the online version, at doi:10.1016/j.cclet.2023.108519.

References

[1] L. Wang, J. Fan, Y. Liu, et al., Adv. Funct. Mater. 31 (2021) 2010912.
[2] Y. Jiang, Y. Li, Y. Jiang, et al., Chin. Chem. Lett. 33 (2022) 4003–4007.
[3] Q. Zhu, B. Qiu, H. Duan, et al., Appl. Catal. B 259 (2019) 118078.
[4] G. Song, Z. Yi, L. Xie, et al., Chin. Chem. Lett. 31 (2020) 1392–1397.
[5] X. Bai, Q. Hou, H. Qian, et al., Appl. Catal. B 303 (2022) 120895.
[6] H.N. Nong, L.J. Falling, A. Bergmann, et al., Nature 587 (2020) 408–413.
[7] K. Sivula, ACS Energy Lett. 6 (2021) 2549–2551.
[8] Y. Li, Y. Wu, H. Hao, et al., Appl. Catal. B 305 (2022) 121033.
[9] Y. Li, W. Wang, B. Zhang, et al., Nano Lett. 21 (2021) 6656–6663.
[10] N. Wang, S. Ning, X. Yu, et al., Appl. Catal. B 302 (2022) 120838.
[11] C. Zhang, R. Du, J.J. Biendicho, et al., Adv. Energy Mater. 11 (2021) 2100432.
[12] F. Chen, Z. Zhang, W. Liang, et al., Chin. Chem. Lett. 33 (2022) 1395–1402.
[13] Z. Xu, S. Jin, M.H. Seo, et al., Appl. Catal. B 292 (2021) 120168.
[14] J. Sun, H. Xue, Q. Wang, et al., Angew. Chem. Int. Ed. 60 (2021) 19435–19441.
[15] H. Fei, T. Guo, Y. Xin, et al., Appl. Catal. B 300 (2022) 120733.
[16] X. Xiao, X. Wang, X. Jiang, et al., Small 4 (2020) 1900796.
[17] Q. Qian, J. Zhang, J. Li, et al., Angew. Chem. Int. Ed. 60 (2021) 5984–5993.
[18] H. Ding, L. Xu, C. Wen, et al., Chem. Eng. J. 440 (2022) 135847.
[19] H. Ning, G. Li, Y. Chen, et al., ACS Appl. Mater. Inter. 11 (2019) 1957–1968.
[20] D. Wang, W. Gong, J. Zhang, et al., Chin. J. Catal. 42 (2021) 2027–2037.
[21] Y. Li, J. Liu, C. Chen, et al., ACS Appl. Mater. Inter. 9 (2017) 5982–5991.
[22] B.W. Zhang, T. Sheng, Y.D. Liu, et al., Nat. Commun. 9 (2018) 4082.
[23] H. Zhao, Y. Jiang, H. Liu, et al., Appl. Catal. B 277 (2020) 119187.
[24] Z. Jin, P. Li, D. Xiao, et al., Green Chem. 18 (2016) 1459–1464.
[25] L. An, J. Feng, Y. Zhang, et al., Adv. Funct. Mater. 29 (2019) 1805298.
[26] J. Zhang, T. Wang, D. Pohl, et al., Angew. Chem. Int. Ed. 55 (2016) 6702–6707.
[27] R.Q. Li, B.L. Wang, T. Gao, et al., Nano Energy 58 (2019) 870–876.
[28] W. Jin, J. Chen, B. Liu, et al., Small 15 (2019) 1904210.
[29] R. Xu, T. Jiang, Z. Fu, et al., Nano Energy 78 (2020) 105347.
[30] X. Zhou, H. Gao, Y. Wang, et al., J. Mater. Chem. A 6 (2018) 14939–14948.
[31] G. Yuan, J. Bai, L. Zhang, et al., Appl. Catal. B 284 (2021) 119693.
[32] C. Dong, T. Kou, H. Gao, et al., Adv. Energy Mater. 8 (2018) 1701347.
[33] Y. Zhang, L. Tao, C. Xie, et al., Adv. Mater. 32 (2020) e1905923.
[34] Y. Zou, W. Zhang, N. Chen, et al., ACS Nano 13 (2019) 2062–2071.
[35] Y. Zhu, W. Zhou, J. Sunarso, et al., Adv. Funct. Mater. 26 (2016) 5862–5872.
[36] X. Liu, L. Wu, T. Liu, et al., Appl. Catal. B 281 (2021) 119513.
[37] Y. Fang, Y. Zeng, Q. Jin, et al., Angew. Chem. Int. Ed. 60 (2021) 8515–8520.
[38] J. Lin, Y. Yan, T. Xu, et al., J. Colloid Inter. Sci. 564 (2020) 37–42.
[39] J. Liu, R. Meng, J. Li, et al., Appl. Catal. B 254 (2019) 214–222.
[40] Y. Ma, Y. Zhang, M. Xing, et al., Chem. Commun. 58 (2022) 6642–6645.
[41] X. Wang, X. Zong, B. Liu, et al., Small 18 (2022) 2105544.
[42] Z. Wang, Z. Lin, J. Deng, et al., Adv. Energy Mater. 11 (2021) 2003023.
[43] S.B. Pillai, B.A. Baraiya, D. Upadhyay, et al., Int. J. Hydrogen Energy 45 (2020) 23900–23907.
[44] P. Shi, X. Cheng, S. Lyu, et al., Chin. Chem. Lett. 32 (2021) 1210–1214.
[45] H. She, P. Yue, J. Huang, et al., Chem. Eng. J. 392 (2020) 123703.
[46] Y. He, L. Liu, C. Zhu, et al., Nat. Catal. 5 (2022) 212–221.
[47] X. Wang, S. Xi, P. Huang, et al., Nature 611 (2022) 702–708.
[48] H. Cheng, N. Yang, G. Liu, et al., Adv. Mater. 32 (2020) 1902964.
[49] X. Wang, C. Xu, M. Jaroniec, et al., Nat. Commun. 10 (2019) 4876.
[50] X. Yang, X. Gao, M. Jiang, et al., Angew. Chem. Int. Ed. 62 (2023) e202215680.
[51] L. Zhai, X. She, L. Zhuang, et al., Angew. Chem. Int. Ed. 61 (2022) e202116057.